

Cold-temperature deformation of nano-sized tungsten and niobium as revealed by *in-situ* nano-mechanical experiments

LEE Seok-Woo^{1*}, CHENG YinTong¹, RYU Ill² & GREER Julia R.¹

¹Division of Engineering and Applied Science, California Institute of Technology, Pasadena CA 91125, USA;

²School of Engineering, Brown University, Providence RI 02912, USA

Received February 2, 2014; accepted February 28, 2014

We constructed and developed an *in-situ* cryogenic nanomechanical system to study small-scale mechanical behavior of materials at low temperatures. Uniaxial compression of two body-centered-cubic (bcc) metals, Nb and W, with diameters between 400 and 1300 nm, was studied at room temperature and at 165 K. Experiments were conducted inside of a Scanning Electron Microscope (SEM) equipped with a nanomechanical module, with simultaneous cooling of sample and diamond tip. Stress-strain data at 165 K exhibited higher yield strengths and more extensive strain bursts on average, as compared to those at 298 K. We discuss these differences in the framework of nano-sized plasticity and intrinsic lattice resistance. Dislocation dynamics simulations with surface-controlled dislocation multiplication were used to gain insight into size and temperature effects on deformation of nano-sized bcc metals.

dislocation, plasticity, metal, nanopillar, cryogenics

Citation: Lee S W, Cheng Y T, Ryu I, et al. Cold-temperature deformation of nano-sized tungsten and niobium as revealed by *in-situ* nano-mechanical experiments. *Sci China Tech Sci*, 2014, 57: 652–662, doi: 10.1007/s11431-014-5502-8

1 Introduction

Understanding of small-scale plasticity is essential to design the reliable small mechanical devices such as micro-/nano-electro-mechanical systems (MEMS/NEMS) [1]. To meet this need, various experimental techniques have been developed to explore small-scale mechanical properties. For the sample fabrication, focused-ion beam milling, electroplating, and nanowire/nanoparticle growth have been widely used to fabricate samples because it is relatively easy to control the sample dimension, allowing the systematic studies of the size effects on the mechanical properties of materials [2–5]. For the mechanical testing technique, a nanoindenter system, which usually uses a sharp diamond tip to measure the hardness and elastic modulus of thin ma-

terials, adopts a flat punch tip, and uni-axial compression tests has been done by compressing a pillar-shaped sample with the flat top surface [6–8]. Also, tensile testing methods have been extensively developed with advanced sample gripping techniques such as hook-shaped tension grips [9–11], e-beam assisted metallic deposition [12–14], and MEMS-driven designs [15–17]. So far, most of small-scale mechanical tests have been done at room temperature because it does not require the special modification of equipment. However, engineering materials are often used at a temperature other than room temperature. Especially, space or marine applications requires materials to serve at different thermal environments. Due to the advances in nanotechnology, the interests in the use of nanomaterials or MEMS devices under the different thermal environments keep growing [18–20], and it must be necessary to develop the suitable experimental techniques that can evaluate the mechanical properties of small-sized materials at different

*Corresponding author (email: swlee49@caltech.edu)

temperatures.

Recently, several research groups have developed the nanomechanical testing system working at high temperatures. These high temperature systems are suitable to study the size effects on the shape memory effects, dislocation nucleation, indentation size effects, fatigue and creep behaviors [21–25]. However, the low temperature system has not been actively developed, yet. The cryogenic system would be useful particularly for space applications since the space environment is often cryogenic. One of the most expensive requirements in the development of cryogenic system is the ultra-high vacuum (UHV) environment because the vapor condensation on the sample surface or at the inside of electronic system of the indenter head should be avoided. Especially for nano-mechanical testing, the deposition of small amount of different materials on the surface could affect the experimental results significantly. We already have had an *in-situ* nanomechanical testing system installed in the UHV chamber of scanning electron microscope (SEM) [26]. In our previous work, the cryogenic system was installed into our *in-situ* nanomechanical testing system for the first time, and we were able to achieve the relatively low thermal drift by the simultaneous cooling of both the diamond tip and sample (The thermal drift data is available in the supplementary information of ref. [27]). As the first validation of our system, we studied the indentation size effect at different cryogenic temperatures. It was found that the intrinsic lattice resistance and the cross-slip probability are the key physical parameters to govern the temperature-dependent indentation size effects, especially for body-centered-cubic (bcc) metals, W and Nb. These two physical processes are, in general, related to the motion of dislocation, and they could also play an important role in the other types of small-scale plastic deformation, such as uniaxial deformation of metallic micro/nanopillars.

Uniaxial deformation at small length scales has revealed that size-dependent strength and strain burst are two key characteristics in small-scale plasticity [2–5]. Size dependent strength is related to the truncation and exhaustion of dislocation sources, and the strain burst is related to the intermittent dislocation generation/multiplication. The change in temperature could alter these two characteristics in bcc metallic pillars because the dislocation behavior, especially the mobility of dislocation, is generally temperature-dependent. Therefore, it would be interesting to study how the change in temperature affects these two features of small-scale plasticity.

In this paper, we studied the mechanical properties of bcc Nb and W nanopillars at a low temperature. Here, Nb and W nanopillars with the diameter of 400–1300 nm were fabricated using focused-ion beam milling, and uniaxial compression tests were performed at 165 K. The experimental data obtained at 298 K from the same sample will be compared. It is well known that the size dependent strength is characterized by the power law $\sigma = A \cdot D^{-n}$, where σ is

the measured yield or flow strength, A is the proportional factor, D is the pillar diameter, and n is the scaling exponent. The temperature effects on the scaling exponent, n , of the power law will be analyzed for the yield strength and the flow stress at 8% strain. Also, we will discuss how the strain burst size is affected by the change in temperature. A recently developed dislocation dynamics simulation, in which the surface-induced cross-slip had been implemented, was also used to understand both size and temperature effects on the strain burst size.

2 Experimental method

2.1 Cryogenic system set-up

We have developed an *in-situ* cryogenic nanomechanical testing system by combining the nanomechanical tester (InSEMTM, Nanomechanic, inc), SEM (Quanta, FEI), and cryogenic systems (Janis Research Company, LLC) [27]. The schematic diagram in Figure 1 shows that the cryogenic system consists of cold finger, Si-diode temperature sensors, joule heaters, radiation shielded oxygen-free high thermal conductivity copper (OFHC) lines, vacuum shielded coolant transfer line, the liquid nitrogen dewar, and temperature controller. In our previous work, we used the liquid nitrogen to cool down the sample, and 160 K was the minimum obtainable temperature after 10 h cooling. The temperature of liquid nitrogen in the dewar is lower than its boiling temperature, 77 K, and the temperature of the cold finger is near 77 K during cooling (see Figure 3). However, the temperature of sample stage is always much higher than that of cold finger because of the heat conduction from the chamber wall to the sample stage. Also, the radiation from the chamber also supplies the additional heat to the sample stage. Thus, it was challenging to achieve the better cooling condition to reach the temperature lower than 160 K at the sample stage.

In order to obtain the better cooling capability, we recently re-designed the sample stage by using titanium for the better thermal insulation between the sample stage and the chamber wall. Titanium can effectively prevent the heat flow between the sample stage and the chamber due to its low thermal conductivity ($21.9 \text{ Wm}^{-1}\text{K}^{-1}$), which is even lower than alumina ($30 \text{ Wm}^{-1}\text{K}^{-1}$) used in the previous system. Furthermore, the radiation shielded OFHC copper line is added to enhance the heat conduction between the sample stage and the cold finger. Figure 2 shows the photographs of the detailed configuration of cryogenic system. With this new set-up, we were able to obtain 130 K after 10 h cooling as seen in Figure 3. The current temperature controller is able to keep the target temperature within the error, $\pm 0.1 \text{ K}$ by using the proportional-integral-derivative (PID) control of heaters at the cold finger and sample stage. Thus, it is now possible to perform cryogenic nanomechanical tests with the precise temperature control between 130 K and 298 K with

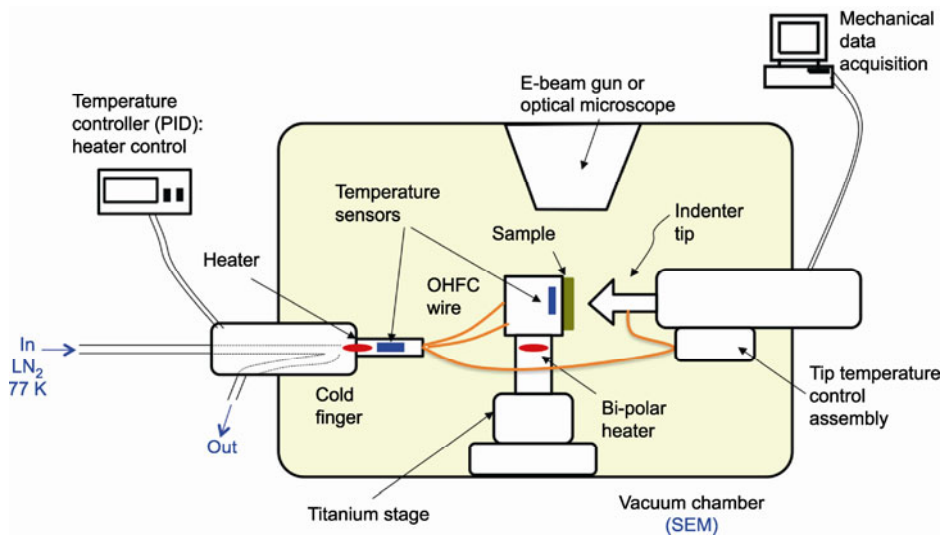


Figure 1 (Color online) Schematic diagram of an *in-situ* nanomechanical tester integrated with the cryogenic system.

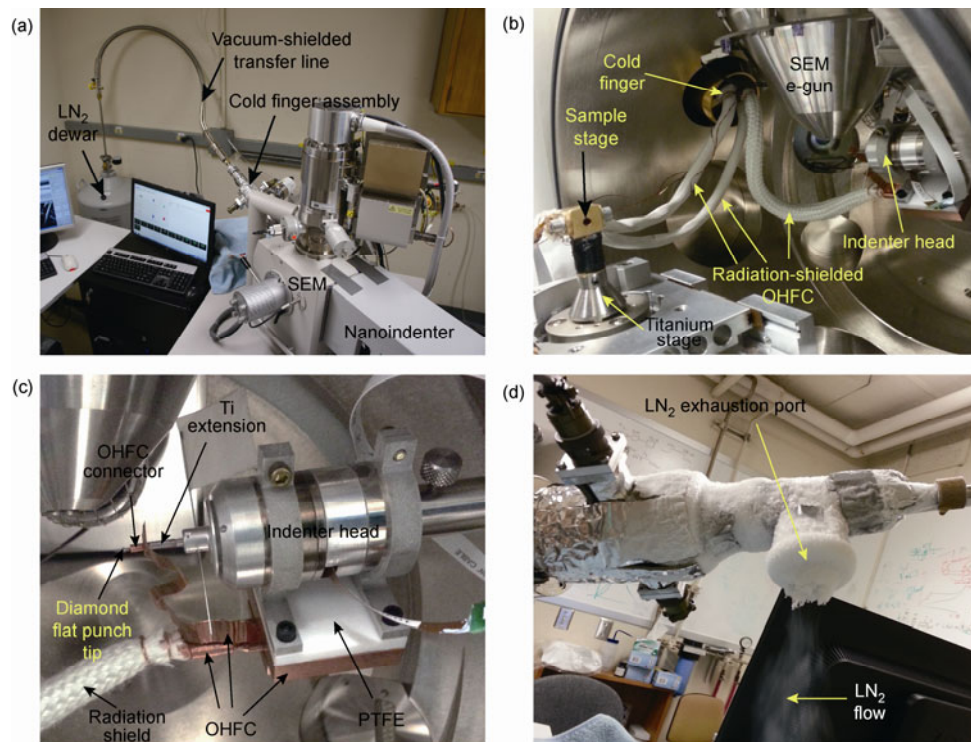


Figure 2 (Color online) Photographs of (a) the chamber outside, (b) the chamber inside, (c) the indenter head assembly, and (d) the exhaustion port of liquid nitrogen.

our current set up.

The low temperature test has some benefits to study the temperature effects on the small-scale plasticity, compared to the high temperature test. For instance, at a high temperature, the surface diffusion of atoms could affect the deformation behavior at the nanoscale because surface diffusion could alter the sample shape even below the melting temperature of bulk materials [28]. Furthermore, vacancy diffusion could cause the climb motion of edge dislocation [29]. Thus, the diffusional process could make the interpretation

of the deformation behavior more difficult at high temperatures. At cryogenic temperatures, in contrast, the diffusional processes are not significant, leading to the simpler study of temperature-dependent behavior of dislocations at small length scales.

2.2 Sample fabrication and mechanical tests

Nanopillars with the diameter of 400–1300 nm were fabricated from bulk Nb and W single crystals by using focused

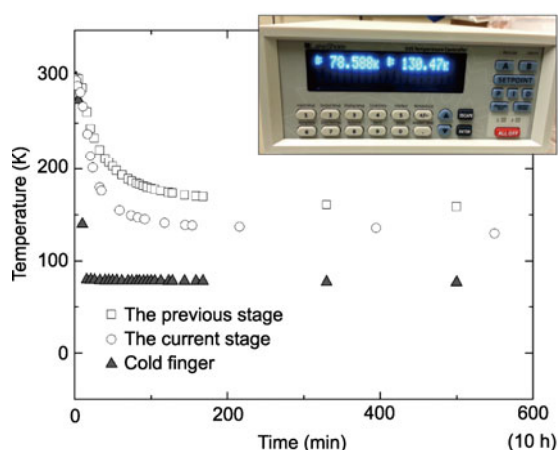


Figure 3 (Color online) The temperature profiles with time for both the previous [27] and the current systems. The temperature of the cold finger is close to 77 K regardless of the sample stage design. The inset image shows that the temperature of the cold finger (left) and that of the sample stage (right).

ion-beam milling (Dual Beam Nova 200, FEI). Note that the diameter reported in this paper is the average diameter measured in the middle height of the pillar. Final milling was done with 10–30 pA of Ga⁺ ion beam under 30 kV. Both Nb and W nanopillars are axially oriented along the [0 0 1] direction, and have the similar aspect ratio of the height/diameter, ~3. The concentric pattern milling usually produced the taper with the angle, 2°–4°. The nanopillars with the diameter less than 400 nm were also fabricated, but it was difficult to achieve the reliable mechanical data due to the vibration of indenter tip. The liquid nitrogen flow rate is not constant, resulting in the vibration of SEM chamber. This chamber vibration causes the indenter tip vibration with the amplitude less than 10 nm. Because the velocity of the tip sometimes becomes fast abruptly, the impact causes the non-desired plastic deformation for $D < 400$ nm pillars even before making a full contact. However, for $D > 400$ nm pillar, this impact deformation is within elastic regime. Also, once the tip makes a full contact with the sample, there is no more impact deformation, allowing the stable mechanical tests. This is the reason why the cryogenic data is only available for $D > 400$ nm while the 298 K data includes the nanopillar with $D < 400$ nm in Section 3. Reduction of the tip vibration, which is associated with the liquid nitrogen flow, is the current on-going work.

The uniaxial compression tests were done at 165 K with the nominal displacement rate, 4 nm/s. The thermal drift was measured for 10 s at 20% of the final load, and the measured thermal drift is always less than 0.5 nm/s, which is comparable with that at room temperature of our *in-situ* machine. This result indicates indirectly that there is not much heat flow between the tip and the sample. Thus, the measured temperature of the sample stage is almost same with the temperature of nanopillars. The true stress-strain curves were calculated according to the framework of plastic volume conservation in ref. [7,30]. This assumption is

valid as long as the plastic strain is dominant, as the plastic deformation due to dislocation gliding does not change the volume.

To compare with mechanical data at 165 K, we use the room temperature data taken from the work done with the same sample in ref. [31]. In this previous work, the nominal displacement rate of 2 nm/s was used. It is twice slower than the rate in this study (4 nm/s) but the only twice difference in displacement rate would change the stress level less than 1% for the low strain rate regime, 10^{-3} s⁻¹ [32], which is the same order of magnitude in our study (10^{-3} – 4×10^{-3} s⁻¹). Thus, here, there is no significant strain rate effect. Also, note that the room temperature data is taken from the different instrument (Dynamic Controlled Module (DCM) of G200, Agilent Technology). However, we also used the DCM head with the similar displacement control in our *in-situ* machine. For both systems, the each strain burst of nanopillars is not stopped by the displacement control but by the microstructural change because the microstructural evolution rate is much faster than the PID loop response. We also tested a Nb pillar with $D \sim 300$ nm at 298 K with the current *in-situ* system, and we got similar size distribution of strain bursts (not shown here) with that of G200. Thus, the difference in stress-strain curves between 298 K and 165 K, especially strain burst size, does not come from the difference in machine, but purely from the temperature effects.

3 Results

3.1 Slip behavior of Nb and W nanopillars

The SEM images of deformed nanopillars in Figure 4 show that Nb exhibits more sharp and localized slip traces, but W exhibits more uniform deformation at 160 K. Kim et al. [31] and Schneider et al. [33] observed the similar slip features at room temperature. These results would be related to the cross-slip process of screw dislocation. W has the critical temperature higher than Nb, which indicates that the screw dislocation mobility is much slower than the edge dislocation mobility [33]. In W nanopillars, the edge component of dislocations moves faster toward the free surface than the slow screw component. Then, the edge component could be more rapidly annihilated at the free surface, and most dislocations in a W nanopillar would be screw-type dislocations, which could cross-slip and could lead to more complicated (more uniform) plastic deformation behaviors. In Section 4.2, dislocation dynamics simulation results will also demonstrate the similar feature.

3.2 Suppression of size effects on the yield strength at 165 K

Figure 5 shows the stress-strain curves of Nb and W nanopillars obtained at 165 K and room temperature. Here, we defined the yield strength as the stress level at which the

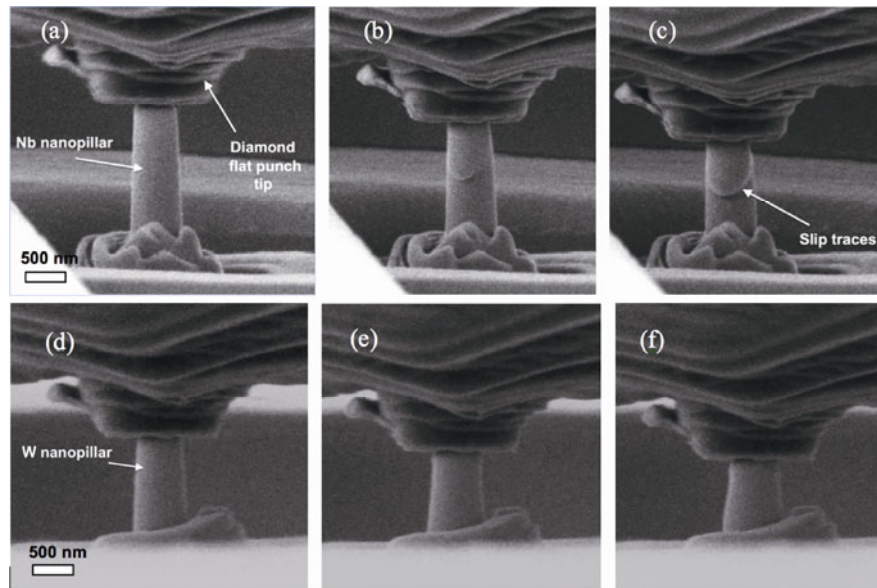


Figure 4 Snapshots of *in-situ* compression of (a)–(c) Nb and (d)–(f) W nanopillar with $D \sim 600$ nm at 165 K. The Nb nanopillar shows more localized deformation than W.

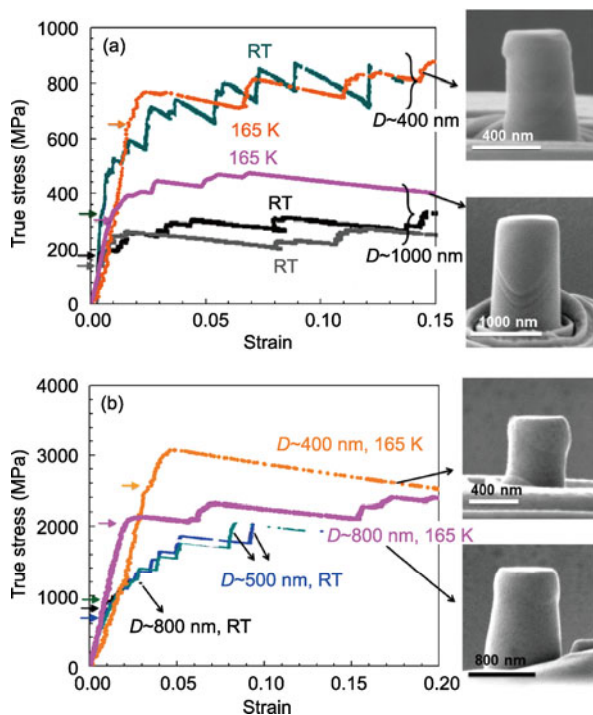


Figure 5 Stress-strain curves at room temperature [31] and at 165 K, and SEM images of (a) Nb and (b) W nanopillars taken at 165 K. The arrows indicate the place where the yield strengths were measured (reprinted with the permission of Kim et al. [31]).

first elastic-to-plastic transition occurs, and it is indicated by arrows in Figure 5. Figure 6(a) shows the size dependence of the yield strength. The yield strengths of both materials are always higher at 165 K than those at 298 K for a given diameter. These results make sense because the intrinsic lattice resistance of bcc crystals is usually higher at lower

temperature, resulting in the higher required stress for the motion of dislocation, i.e., the operation of dislocation sources. The size effect has been analyzed for both yield strength and flow stress at 8% strain based on the power law, $\sigma = A \cdot D^{-n}$ in Figure 6. Figure 6(a) shows clearly that the size effects on the yield strength are suppressed at lower temperature. For Nb, the scaling exponent is 0.73 at room temperature, but is 0.36 at 165 K, which is almost 50% reduction. For W, the scaling exponent is 0.28 at room temperature, but is 0.19 at 165 K, which is 32% reduction. Similar temperature dependence of scaling exponent was also reported for Mo micropillar compression tests at high temperatures [34]. These results correspond to the theoretical expectation done in Lee and Nix [35]. The intrinsic lattice resistance is the size-independent component in the stress required for the operation of dislocation source. Then, the higher intrinsic lattice resistance brings out the lower size dependence on the yield strength. The more quantitative analysis of the effects of the intrinsic lattice resistance will be discussed in Section 4.1.

3.3 Bigger strain burst at 165 K in a smaller nanopillar

The flow stresses at 8% strain at 165 K were measured with diameter, and compared with those at 298 K in ref. [31]. Figure 6(b) shows that the flow stress at 8% strain exhibits the similar temperature dependence with that of the yield strength. That is, the size effect is suppressed at 165 K. For Nb, the scaling exponent decreased from 0.92 to 0.16, and for W, from 0.42 to 0.04. If the flow stress at 8% strain is compared with the yield strength for both 165 and 298 K, the temperature effects on the work hardening rate in the early stage of plastic deformation can be understood. Note

that for the smaller size near $D \sim 400$ nm, the flow stress at 165 K is close to that at 298 K. These results indicate that the work hardening rate at 165 K is much lower than that at 298 K, especially for the smaller pillars. The main reason for the lower strain-hardening rate at 165 K is the large strain burst size at low temperatures as seen in stress-strain curves in Figure 5. The deformation behavior during strain burst is almost perfect plastic, resulting in the near-zero work hardening rate. Therefore, the series of the large strain bursts at 165 K produces the low overall work hardening rate. The large strain burst indicates that once the dislocation activity begins, this activity continues for a longer time at a low temperature, compared to that at 298 K.

Furthermore, note that especially for $D \sim 1000$ nm Nb pillars, the work hardening rate is low for both 298 and 165 K as seen in Figure 5(a). This indicates that dislocations can generate large strain burst even at 298 K when the sample size is large enough. A dislocation dynamics simulation is particularly useful to understand the dislocation motion in a nanopillar. The temperature effects on the strain burst size will be discussed with the recently developed dislocation dynamics code in Section 4.2.

4 Discussion

4.1 Temperature effects on the yield strength of nanopillars

For a given stress condition, the mobility of screw dislocation gets slower at a lower temperature because the nucleation of double-kink gets more difficult with the lower supplied thermal energy, resulting in the higher required stress for the operation of dislocation source. If we define the yield strength as the first elastic-to-plastic transition point in a stress-strain curve, the yield strength corresponds to the stress level required for the operation of the weakest dislocation source. Typically, the source operation stress is represented as

$$\sigma_i = \frac{1}{M} \left(\tau_0 + 0.5\mu b \sqrt{\rho_{\text{tot}}} + \frac{\alpha\mu b}{\lambda_i} \right), \quad (1)$$

where M is the Schmidt factor, τ_0 is the intrinsic lattice resistance, b is the magnitude of Burgers vector, μ is the shear modulus, ρ_{tot} is the total dislocation density, α is a factor with the order of unity, and λ is the length of the i -th dislocation source [35–37]. The number of dislocation source (n) is defined as

$$n = \text{Int} \left[\rho_{\text{tot}} \cdot \left(\frac{\pi D^2}{4} \right) \cdot \frac{1}{D} \right], \quad (2)$$

where D is the pillar diameter, with assuming that the average length of individual dislocation source is D . The numerical method to calculate λ is available in ref. [35–37], and the materials parameters are obtained from ref. [35]. With the stochastic numerical approach, the lowest σ_i can be obtained as the yield strength of nanopillars for a given dislocation density and pillar diameter. For face-centered cubic (fcc) metallic pillars, the intrinsic lattice resistance is usually ignored because the mobility of dislocation is relatively high. However, for bcc pillars, the intrinsic lattice resistance cannot be neglected due to the low mobility of screw dislocation. With eq. (1), it is possible to estimate the intrinsic lattice resistance by matching numerical results with the experimental results in Figure 6(a).

We simulated 500 pillars for each diameter with the dislocation density, 10^{13} m^{-2} , and averaged it to get the yield strength of pillars for each diameter. Figure 7 shows both experimental and calculated data for four different intrinsic lattice resistance. Ten calculations were done with the resolution of τ_i of 20 MPa for Nb and 50 MPa for W, but Figure 7 includes only four cases for each material to avoid making figures look busy. We found that the intrinsic lattice resistances of Nb and W nanopillars at 298 K have ~ 98 MPa and ~ 735 MPa, respectively, and at 165 K, ~ 294 MPa and

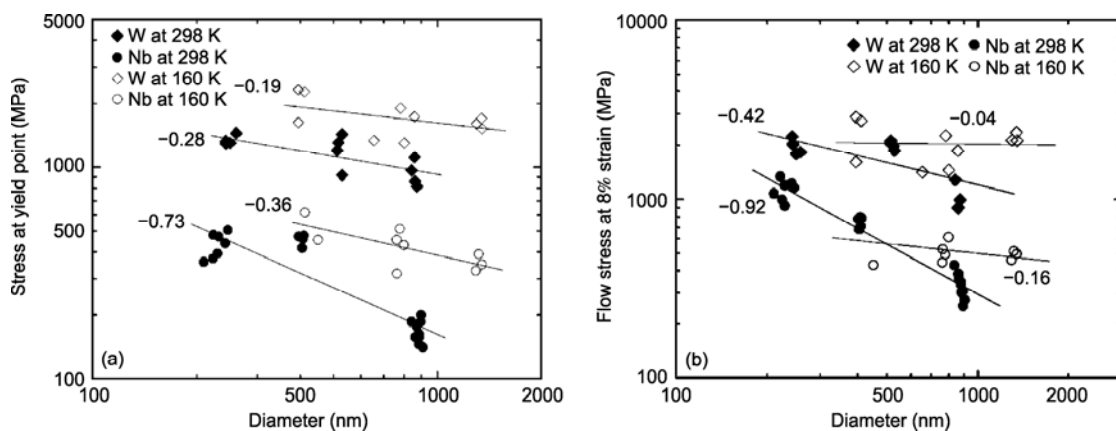


Figure 6 The scaling plot of (a) yield strength and (b) flow stress at 8% strain at 298 K and 165 K (Reprinted with the permission of Kim et al. [31]).

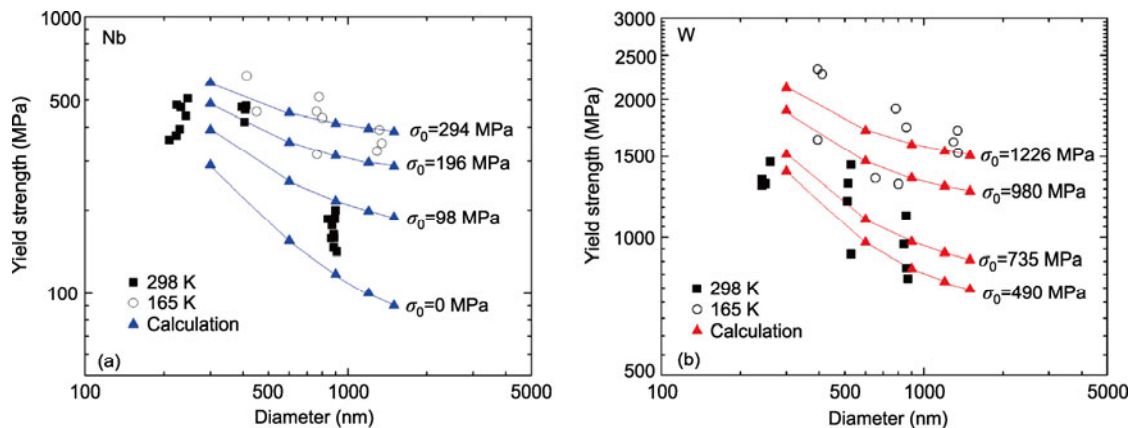


Figure 7 (Color online) Size-dependent yield strength of (a) Nb and (b) W obtained from experiments and calculations.

~1226 MPa, respectively. Thus, these results show that the intrinsic lattice becomes much higher at 165 K than that at 298 K. Also, Figure 7 shows that the size dependence is much weaker at 165 K than at 298 K. This indicates that the higher intrinsic lattice resistance is the major reason for the suppression of size effects observed in Figure 6. In eq. (1), the first term, τ_0 , is the size-independent term, and the third term, $\alpha\mu b/\lambda_i$, is the size-dependent term. Thus, the competition between these two terms controls the size dependence of the strength. At a low temperature, τ_0 is much higher than $\alpha\mu b/\lambda_i$, leading to the weak size dependence in eq. (1).

In other literatures, the intrinsic lattice resistance of bulk Nb and W at 298 K are 46 MPa [38] and 600 MPa [39], respectively and at 165 K, 269 MPa [38] and 1034 MPa [39], respectively. Note that the reported bulk values are relatively similar with our calculation, but always slightly smaller than those in this work. This result would come generally from the larger fraction of screw dislocation in a nanopillar, compared to a bulk material. As described in Section 3, in a small volume, the fast edge component could be more rapidly annihilated than the slow screw component. Then, the majority of dislocations would be screw-type in nanopillars. Because the screw dislocation has the higher intrinsic lattice resistance than the edge dislocation, the average intrinsic lattice resistance would be higher in a nanopillar than that in a bulk material, which is consistent with our observation. Deformed crystalline Mo with the grain size comparable with our nanopillar size also exhibits the screw dislocation density much higher than the edge/mixed dislocation density in the postmortem observation [40] due to the rapid annihilation of edge dislocation. Thus, the screw dislocation governs mechanical properties with the length scale of this study.

4.2 Dislocation dynamics simulation study on the relation between temperature and strain burst size

Figure 5 shows that the strain burst size is significantly larger at 165 K for both Nb and W nanopillars with D -

400 nm, compared to that at 298 K. This indicates that the dislocation activity for each strain burst is much more pronounced at a lower temperature. In other words, a dislocation source could generate more number of dislocations at a lower temperature. One of the unique plasticity mechanisms of dislocations in bcc nanopillars is the surface-controlled dislocation multiplication [41,42]. For a particular orientation of screw dislocation, the image stress induces cross-slip at the free surface, leading to the unusual dislocation multiplications, which does not occur in bulk metals. Thus, it is interesting to see how the temperature change affects dislocation multiplication in bcc nanopillars. In general, the temperature affects the mobility of screw dislocation. Thus, we studied the effect of screw dislocation mobility on surface-controlled dislocation multiplication with the use of the dislocation dynamics (DD) simulation code, ParaDiS (Parallel Dislocation Simulator, Lawrence Livermore National Laboratory), where the rules of surface-controlled dislocation multiplication were already implemented [43].

4.2.1 Mobility parameters

The dislocation velocity depends on both temperature and stress state. We assume the simple linear mobility law, which is $v = M \cdot f$, where v is the velocity of dislocation node, M is the mobility parameter and f is the force on a dislocation node. Here, M is the strong function of temperature and f is the function of stress state. In this study, the mobility parameter is the important quantity because the change in temperature affects the mobility of screw dislocation. Accurate calculation of mobility parameters with the higher-level computations, such as molecular dynamics simulation, would be beneficial. In our case, however, the relative mobility parameters are more important than the absolute values because the difference between screw and edge mobility is the key factor to control the surface-induced dislocation multiplication.

First, we performed two different mobility cases, $M_{\text{edge}} = M_{\text{screw}}$ and $M_{\text{edge}}/100 = M_{\text{screw}}$ for the diameter of 500 nm to see the effect of the relative difference in dislocation mobil-

ity on the surface-controlled dislocation multiplication. The former condition corresponds to the high temperature such that the temperature is similar with the critical temperature at which, by definition, the mobility of screw dislocation becomes same with that of edge dislocation. This condition would work for Nb at room temperature because the critical temperature of Nb, 350 K, is relatively close to 298 K [33]. The latter condition would be close to Nb at a low temperature because the mobility of screw dislocation would be much smaller than that of edge dislocation at a lower temperature.

According to molecular dynamics simulations, Mo has the mobility of screw dislocation one hundred times smaller than that of edge dislocation at 298 K [41]. The critical temperature of Mo is 480 K, which is 182 K higher than room temperature (298 K) [33]. Our cryogenic experimental temperature, 165 K, is nearly 190 K smaller than the critical temperature of Nb, 350 K. As the first order approximation, if we assume the similar temperature dependence of the relative mobility, the mobility of screw dislocation in Nb would also become approximately one hundred times smaller than the edge dislocation. Thus, the condition, $M_{\text{edge}}/100 = M_{\text{screw}}$, would be not the bad assumption of mobility at 165 K for Nb. W would have much lower mobility of screw dislocation at 165 K because W has the high critical temperature, 800 K [33]. In this work, we simply use the condition, $M_{\text{edge}}/100 = M_{\text{screw}}$, to demonstrate how the relative dislocation mobility affects the surface-controlled dislocation multiplication. Material parameters of Nb were taken from ref. [35], and the radius of non-singular dislocation core, r_c , was chosen as b , where b is the magnitude of Burgers vector, as done in ref. [41].

4.2.2 Force calculations

For the simplicity of simulation, the line-tension-like approach is used. Thus, our simulation includes the self-force, the elastic interaction force, the Peach-Koehler force due to the applied stress, and no image stress. The self-force and the elastic interaction force were calculated in the framework of the non-singular continuum theory [44]. As noted in ref. [41], surface-induced cross-slip occurs by the tendency that the dislocation wants to be shorter to minimize the total elastic energy, and the self-force in our model drives this tendency. Thus, it is possible to capture the surface-induced cross-slip without the expensive computation of image stresses. In fact, it would be difficult to obtain the accurate image stress on the small cross-slipped segment attached at the free surface. Thus, the line tension approach provides the much simpler way to study the surface-controlled dislocation multiplication.

4.2.3 Initial dislocation geometry

The initial configuration of dislocation is shown in Figure 8(a). The screw dislocation is initially on the $(0\ 1\ \bar{1})$ plane. Both dislocation line and Burgers vector are oriented along

the $[1\ 1\ 1]$ direction. At the beginning of simulation, the surface cross-slip is always occurs on the surface node B only. For the given initial configuration, the self-force is symmetric along the line. Thus, the surface-induced cross-slip would occur on both the surface nodes, A and B. However, the Peach-Koehler force cancels out the self-force on the surface node A while it enhances the self-force on the surface node B. In Figure 8(b), the arrow indicates the resolved forces on the $(1\ 0\ \bar{1})$ plane. Thus, the surface-induced cross-slip does not occur for the surface node A, and the surface node B cross-slips from the $(0\ 1\ \bar{1})$ to the $(1\ 0\ \bar{1})$ plane. Thus, after a few time steps, we can see a single dislocation on two different slip planes as seen in Figure 8(c).

4.2.4 The temperature effects on the surface-controlled dislocation multiplication

First, for $D \sim 500$ nm Nb nanopillar, the constant stress, 350 MPa, was applied along the axial direction. Figure 9 shows that for $M_{\text{edge}} = M_{\text{screw}}$, the screw dislocation rotates around the cusp, first. The dynamic pinning point, where two dislocations on the different slip planes meet, migrates towards the free surface, and the whole dislocation is annihilated at the free surface. Thus, the dislocation does not multiply, and cannot produce the large plastic strain. For $M_{\text{edge}}/100 = M_{\text{screw}}$, however, the edge dislocation is much faster than screw dislocation. Figure 10 shows that the two edge dislocations of the cusp move towards the free surface rapidly, leading to the expansion of the cusp. When two edge dislocations are annihilated at the free surface, three dislocations remain in the pillar. This process can be repeated many times because the new dislocations are also near screw-type, leading to the surface-controlled dislocation multiplication.

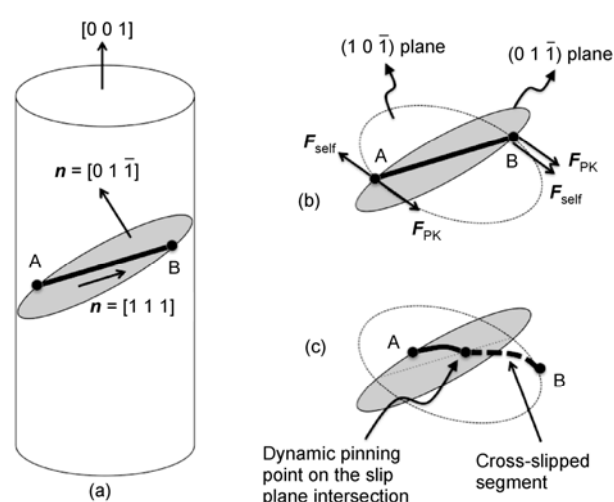


Figure 8 (a) Initial configuration of pure screw dislocation; (b) the self-forces and the Peach-Koehler forces that are resolved on the $(1\ 0\ \bar{1})$ plane, here, the length of arrow does not represent the magnitude of force; (c) the dislocation structure after surface-induced cross-slip. The cross-slipped dislocation is on $(1\ 0\ \bar{1})$ plane, but the original dislocation is on the $(0\ 1\ \bar{1})$ plane.

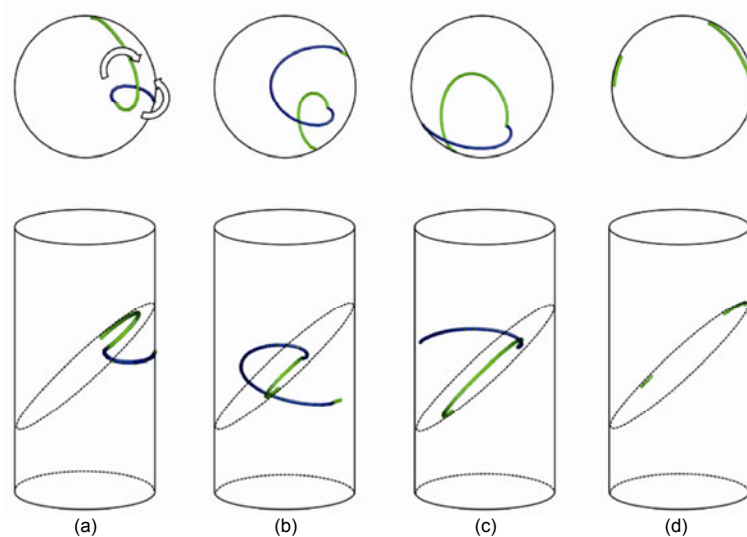


Figure 9 Dislocation motion with surface-induced cross slip for $M_{\text{edge}} = M_{\text{screw}}$ under the axial stress, 350 MPa, in $D \sim 500$ nm Nb nanopillar. The top four figures show the top view of nanopillars, and the bottom four figures show the side view of nanopillars. The dotted line indicates the original slip plane on which the initial dislocation stays. The dislocation is completely annihilated as seen in Figure 9(d).

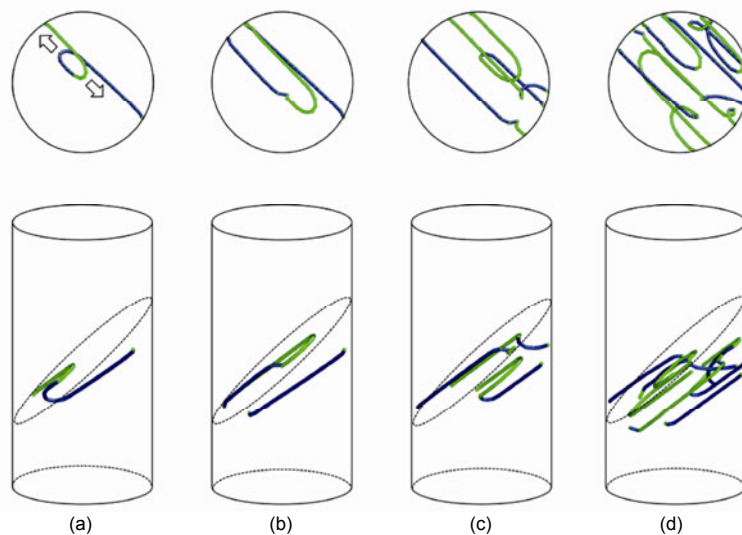


Figure 10 Dislocation motion with surface-induced cross slip for $M_{\text{edge}}/100 = M_{\text{screw}}$ under the axial stress, 350 MPa, in $D \sim 500$ nm Nb nanopillar. The arrows in Figure 10(a) show the motion of two opposite edge dislocation towards the free surface.

In this study, dislocation dynamics simulation shows that the surface-controlled dislocation multiplication requires the lower mobility of screw dislocation than that of edge dislocation. Two edge dislocations of the cusp must arrive at the free surface before the screw dislocation rotates around the dynamic pinning point. This condition could be achieved at a lower temperature more easily because the double-kink cannot be nucleated easily, leading to the lower mobility of screw dislocations. Therefore, at lower temperature, the surface-induced multiplication could occur more actively, and could produce the larger strain burst as seen in the stress-strain curves of Figure 5. Also, note that the applied stress level, 350 MPa is lower than the yield strength of Nb

nanopillar with the same diameter in experiment at 165 K. Thus, the surface-controlled dislocation multiplication would be available after yield point at 165 K.

4.2.5 The size effects on the operation of dynamic dislocation source

A screw dislocation in $D \sim 1000$ nm Nb pillar was also studied for $M_{\text{edge}} = M_{\text{screw}}$. Here, the constant stress, 250 MPa, was applied along the axial direction. Note that this stress level is lower than the flow stress at 8% strain, ~ 300 MPa, at room temperature. In the case of $D \sim 500$ nm pillar, the dynamic pinning point, i.e., the dislocation node where two dislocations on different slip planes meet, move early out of

the free surface. Due to the smaller diameter, the dislocation moves out quickly before source operation. Also, the source operation also required the higher stress due to the higher line tension force, which is typically inversely proportional to the diameter (or source length). For $D \sim 1000$ nm, however, Figure 11 shows that the dynamic pinning point can stay for a longer time because the sample dimension is bigger. Even though the surface multiplication is not operative, dislocations can produce large plastic strains by rotating motion around the pinning point. Thus, in a larger pillar, dynamic dislocation source can operate for a longer time, compared to the smaller pillar. This result is consistent with the large strain burst in Nb even at room temperature. Also, we did not study the dislocation interaction in this work, but in a large volume, multiple dislocations can interact with each other, leading to the conventional dislocation multiplication. Thus, in a large volume, the strain burst size could be larger even though the surface-controlled dislocation multiplication does not occur.

5 Concluding remarks

1) We have developed an *in-situ* cryogenic nanomechanical testing system to study the small-scale mechanical behavior of materials at low temperatures. With the re-designed sample stage and additional OFHC copper line, the current cryogenic system has the capability to reduce the sample temperature down to 130 K. The simultaneous cooling of both a sample and diamond tip ensures the reliable mechanical tests with the low thermal drift < 0.5 nm/s, comparable with that at room temperature.

2) In this study, nanopillars with the diameter of 400–

1300 nm were fabricated from two body-centered-cubic metals, Nb and W, and uniaxial compression tests were done at 165 K to study the temperature-dependent size effects on their mechanical behaviors. Stress-strain curves at 165 K exhibit the higher yield strengths and larger strain burst sizes than those at 298 K.

3) Based on the numerical calculation of single arm source model, we obtained the intrinsic lattice resistance of Nb and W as 98 and 735 MPa at 298 K, respectively, and 294 and 1226 MPa at 165 K, respectively. Thus, the intrinsic lattice resistance is obviously higher at 165 K due to the low mobility of dislocations at a low temperature. Also, it leads to the lower scaling exponent of the power law ($\sigma = A \cdot D^{-n}$) for yield strengths. Nb shows 0.73 at 298 K and 0.36 at 165 K. W exhibits the scaling exponent of 0.28 at RT and 0.19 at 165 K. Thus, the intrinsic lattice resistance is the main parameter to control the temperature dependence of scaling exponent.

4) Dislocation dynamics simulations were done with two different mobility conditions, $M_{\text{edge}} = M_{\text{screw}}$ and $M_{\text{edge}}/100 = M_{\text{screw}}$. For $D \sim 500$ nm, When the mobility of screw dislocation is similar with that of edge dislocation, the surface-controlled dislocation multiplication is limited, and cannot be continued. However, when the mobility of screw dislocation is smaller than that of edge dislocation, the surface-controlled dislocation multiplication occurs well, resulting in the large plastic strain. This result is consistent with our experimental observation showing that the strain burst size is larger at a lower temperature. The latter condition corresponds to the lower temperature since the mobility of screw dislocation is usually reduced by the decrease in temperature. For a large diameter, $D \sim 1000$ nm, the dislocation source could operate relatively stably even though the

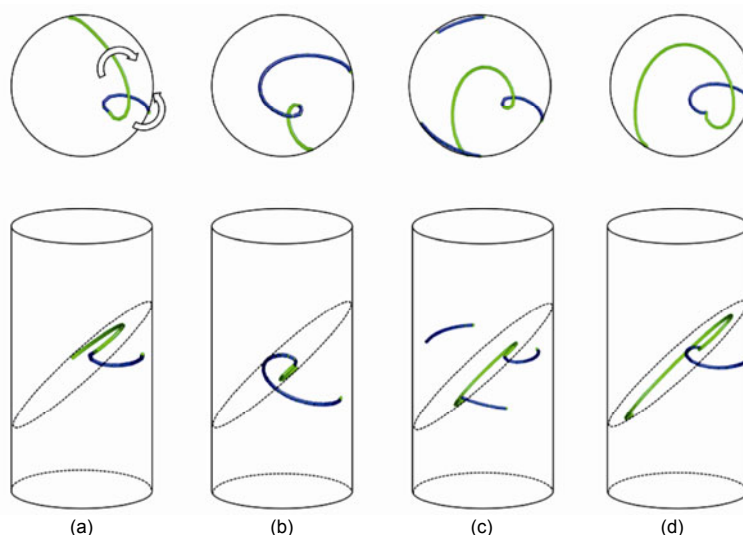


Figure 11 Dislocation motion with surface-induced cross slip for $M_{\text{edge}} = M_{\text{screw}}$ under the axial stress, 250 MPa, in $D \sim 1000$ nm Nb nanopillar. Figure 11(d) looks similar with Figure 11(a), indicating that the source operation can be repeated and can produce large plastic strain even for the condition, $M_{\text{edge}} = M_{\text{screw}}$, in a large pillar.

surface-controlled dislocation multiplication does not occur. The large diameter ensures the longer lifetime of the dynamic pinning point of dislocations.

The authors gratefully acknowledge the financial support of the Kavli Nanoscience Institute (KNI) through LEE Seok-Woo's prized post-doctoral fellowship, of the Keck Institute for Space Studies at Caltech, and of JRG's NASA Early Career grant. CHENG YinTong acknowledges the financial support of the Caltech SURF program.

- 1 Nix W D, Greer J R, Feng G, et al. Deformation at the nanometer and micrometer length scales: Effects of strain gradients and dislocation starvation. *Thin Solid Films*, 2007, 515: 3152–3157
- 2 Uchic M D, Shade P A, Dimiduk D M. Plasticity of micrometer-scale single crystals in compression. *Annu Rev Mater Res*, 2009, 39: 361–386
- 3 Kraft O, Gruber P A, Mönig R, et al. Plasticity in confined dimensions. *Annu Rev Mater Res*, 2010, 40: 293–317
- 4 Zhu T, Li J. Ultra-strength materials. *Prog Mater Sci*, 2010, 55: 710–757
- 5 Greer J R, De Hossien J T M. Plasticity in small-sized metallic systems: Intrinsic versus extrinsic size effect. *Prog Mater Sci*, 2011, 56: 654–724
- 6 Uchic M D, Dimiduk M D, Florando J N, et al. Sample dimensions influence strength and crystal plasticity. *Science*, 2004, 305: 986–989
- 7 Greer J R, Oliver W C, Nix W D. Size dependence of mechanical properties of gold at the micron scale in the absence of strain gradients. *Acta Mater*, 2005, 53: 1821–1830
- 8 Volkert C A, Lilleodden E T. Size effects in the deformation of sub-micron Au columns. *Phil Mag*, 2006, 86: 5567–5579
- 9 Kim J Y, Jang D, Greer J R. Insight into the deformation behavior of niobium single crystals under uniaxial compression and tension at the nanoscale. *Scripta Mater*, 2009, 61: 300–303
- 10 Jang D, Greer J R. Transition from a strong-yet-brittle to a stronger-and-ductile state by size reduction of metallic glasses. *Nature Mater*, 2010, 9: 215–219
- 11 Jang D, Li X, Gao H, et al. Deformation mechanisms nanotwinned metal nanopillars. *Nature Nanotech*, 2012, 7: 594–601
- 12 Richter G, Hillerich K, Gianola D S, et al. Ultra high strength single crystalline nanowhisker grown by physical vapor deposition. *Nano Lett*, 2009, 9: 3048–3052
- 13 Mompou F, Legros M, Sedlmayr A, et al. Source based strengthening of sub-micrometer Al fibers. *Acta Mater*, 2012, 60: 977–983
- 14 Chisholm C, Bei H, Lowry M B, et al. Dislocation starvation and exhaustion hardening in Mo alloy nanofibers. *Acta Materialia*, 2012, 60: 2258–2264
- 15 Kumar S, Li X, Haque A, et al. Is stress concentration relevant for nanocrystalline metals? *Nano Lett*, 2011, 11: 2510–2516
- 16 Kang W, Saif M T A. *In situ* study of size and temperature dependent brittle-to-ductile transition in single crystal silicon. *Adv Func Mater*, 2013, 23: 713–719
- 17 Yilmaz M, Kysar J W. Monolithic integration of nanoscale tensile specimens and MEMS structures. *Nanotechnology*, 2013, 24: 165502
- 18 Azevedo R G, Jones D G, Jog A V, et al. A SiC MEMS resonant strain sensor for harsh environment applications. *IEEE Sensors J*, 2007, 7: 568–576
- 19 Myers D R, Chen L, Wijesundara M B J, et al. Silicon carbide resonant tuning fork for microsensing applications in high-temperature and high G-shock environments. *J Micro/Nanolith MEMS MOEMS*, 2009, 8: 021116
- 20 Zamkotsizn F, Grassi E, Waldis S, et al. Interferometric characterization of MOEMS devices in cryogenic environment for astronomical instrumentation. In: *Proc SPIE 6884, Reliability, Packaging, Testing, and Characterization of MEMS/MOEMS VII*, 68840D, San Jose, 2008, <http://dx.doi.org/10.1117/12.768410>
- 21 Trenkel, J C, Packard C E, Schuh C A. Hot nanoindentation in inert environments. *Rev Sci Instrum*, 2010, 81: 073901
- 22 Juan S J, N6 M L, Schuh C A. Thermomechanical behavior at the nanoscale and size effects in shape memory alloys. *J Mater Res*, 2011, 26: 2461–2469
- 23 Schuh C A, Mason J K, Lund A C. Quantitative insight into dislocation nucleation from high-temperature nanoindentation experiments. *Nature Mater*, 2005, 4: 617–621
- 24 Franke O, Trenkle J, Schuh C A. Temperature dependence of the indentation size effect. *J Mater Res*, 2010, 25: 1225–1229
- 25 Namazu T, Isono Y. High-cycle fatigue test of nanoscale Si and SiO₂ wires based on AFM technique. In: *Micro Electro Mechanical Systems IEEE*, Kyoto, 2003. 662–665, <http://dx.doi.org/10.1109/MEMSYS.2003.1189836>
- 26 Greer J R, Kim K Y, Burek M J. In-situ mechanical testing of nanoscale single crystalline nano-pillars. *Jom*, 2009, 61: 19–25
- 27 Lee S W, Meza L R, Greer J R. Cryogenic nanoindentation size effect in [0 0 1]-oriented face-centered cubic and body-centered cubic single crystals. *App Phys Lett*, 2013, 103: 101906
- 28 Lowry M B, Kiener D, LeBlanc M M, et al. Achieving the ideal strength in annealed molybdenum nanopillars. *Acta Mater*, 2010, 58: 5160–5167
- 29 Hirth J P, Lothe J. *Theory of Dislocations*. 2nd ed. New York: McGraw-Hill, 1982. 559–569
- 30 Lee S W, Han S M, Nix W D. Uniaxial compression of fcc Au nanopillars on an MgO substrate: The effects of prestraining and annealing. *Acta Mater*, 2009, 57: 4404–4415
- 31 Kim J Y, Jang D, Greer J R. Tensile and compressive behavior of tungsten, molybdenum, tantalum, and niobium at the nanoscale. *Acta Mater*, 2010, 58: 2355–2363
- 32 Nemat-Nasser S, Guo W. Flow stress of commercially pure niobium over a broad range of temperatures and strain rates. *Mater Sci Eng A*, 2000, 294: 202–210
- 33 Schneider A S, Kaufmann D, Clark B G, et al. Correlation between critical temperature and strength of small-scale bcc pillars. *Phys Rev Lett*, 2009, 103: 105501
- 34 Schneider A S, Frick C P, Arzt E, et al. Influence of test temperature on the size effect in molybdenum small-scale compression pillars. *Phil Mag Lett*, 2013, 93: 331–338
- 35 Lee S W, Nix W D. Size dependence of the yield strength of fcc and bcc metallic micropillars with diameters of a few micrometers. *Phil Mag*, 2012, 92: 1238–1260
- 36 Parthasarathy T A, Rao S I, Dimiduk D M, et al. Contribution to size effect of yield strength from the stochastic of dislocation source lengths in finite samples. *Scripta Mater*, 2007, 56: 313–316
- 37 Ng K S, Ngan A H N. Breakdown in Schmid's law in micropillars. *Scripta Mater*, 2008, 59: 796–799
- 38 Suzuki T, Koizumi H, Kirchner H K. Plastic flow stress of b.c.c. transition metals and the Peierls potential. *Acta Metall Mater*, 1995, 43: 177–2187
- 39 Raffo P L. Yielding and fracture of tungsten and tungsten-rhenium alloys. *J Less Comm Met*, 1969, 17: 133–149
- 40 Cheng G M, Jian W W, Xu W Z, et al. Grain size effect on deformation mechanism of nanocrystalline BCC metals. *Mater Res Lett*, 2013, 1: 26–31
- 41 Weinberger C R, Cai W. Surface-controlled dislocation multiplication in metal micropillars. *PNAS*, 2008, 105: 14304–14307
- 42 Greer J R, Weinberger C R, Cai W. Comparing the strength of f.c.c. and b.c.c. sub-micrometer pillars: Compression experiments and dislocation dynamics simulations. *Mater Sci Eng A*, 2008, 493: 21–25
- 43 Ryu I, Nix W D, Cai W. Plasticity of bcc micropillars controlled by competition between dislocation multiplication and depletion. *Acta Mater*, 2013, 61: 3233–3241
- 44 Cai W, Arsenlis A, Weinberger C R, et al. A non-singular continuum theory of dislocation. *J Mech Phys Solids*, 2006, 54: 561–587